Journal of ELECTRONIC MATERIALS, Vol. 47, No. 10, 2018
https://doi.org/10.1007/s11664-018-6530-0

Dye-Sensitized Solar Cells Based on an N-Doped TiO_2 and TiO_2-Graphene Composite Electrode

M.A. MOUSA,[1] M. KHAIRY,[1,2,4,5] and H.M. MOHAMED[3]

1.—Chemistry Department, Faculty of Science, Benha University, Benha, Egypt. 2.—Chemistry Department, College of Science, Al-Imam Mohammad Ibn Saud Islamic University, Riyadh, Kingdom of Saudi Arabia. 3.—Chemistry Department, Faculty of Science, Zagazige University, Zagazig, Egypt. 4.—e-mail: mohkhairy@fsc.bu.edu.eg. 5.—e-mail: moh_khairy3@yahoo.com

In this work, the effect of graphene and nitrogen doping on the performance of dye-sensitized solar cells of pure TiO_2 was studied. Pure and N-doped TiO_2 nanoparticles were synthesized using a hydrothermal method, while graphene was prepared through the reduction of graphene oxide. The materials were characterized using x-ray diffraction (XRD), x-ray photoelectron spectroscopy (XPS), Fourier-transform infrared spectroscopy (FT-IR), Raman, Brunauer–Emmett–Teller surface area analysis (BET) and ultraviolet-visible (UV-Vis) diffusion reflectance spectroscopy. Nitrogen dopant concentration varied from 0 at.% to 1.57 at.%. The results confirmed that all N-doped samples exhibited pure anatase phase with an average diameter in the range of 7–12 nm. The pore volume and BET surface area increased with the amount of nitrogen in TiO_2. XPS investigation displayed an N1s peak around 397 eV, which suggested N-Ti-O structure in the TiO_2 matrix. Moreover, optical measurements showed that the optical absorption edge of N-doped TiO_2 exhibited a significant shift from ultraviolet to visible light region in comparison with pure TiO_2. Dye-sensitized solar cells (DSSCs) were fabricated using N719 dye and various TiO_2 based photoanodes. The photoanode of N-doped TiO_2 modified with graphene showed the highest energy-conversion efficiency of 6.3%, while the efficiencies of pure and N-doped TiO_2 cells are 0.41% and 1.21%, respectively. The improvement in conversion efficiency of graphene-based DSSC was attributed to the formed electron bridges between TiO_2 and fluorine-doped tin oxide (FTO), which led to a reduction in the recombination rate of electron-hole pairs and an increase in the rate of electron transport.

Key words: N-doped TiO_2, graphene-composites TiO_2, N719, dye-sensitized solar cell

INTRODUCTION

Increases in world population growth produces energy concerns in a wide range of fields. fossil fuels are becoming progressively rare, and the use of fossil energies are damaging to the environment. A considerable measure of methods for substituting fossil fuels has been created in the past. These days, individuals concentrate on sun-powered energy for its exhaust, purity, cheap and adaptable utilization. Solar cells are a type of photovoltaic cells, which create electrical power by converting the energy of light into direct current power by utilizing semiconductors that exhibit a photovoltaic impact. Solar cells run on daylight as their vital energy source. At present, silicon, polycrystalline silicon, and amorphous silicon solar cells represent the mainstream of high volume production cells with each representing almost one third of the market. Alternatively, dye-sensitized solar cells (DSSCs) have been widely studied for a long time since their introduction by Grätzel and colleagues.[1,2] As a distinct

(Received December 18, 2017; accepted July 17, 2018; published online July 26, 2018)

promising option for conventional electrochemical devices, DSSCs have been studied because of their minimal fabrication effort, stable performance and straightforward assembling procedures.[1–3]

DSSCs consist of the following three parts: (i) a dye-sensitized, nanocrystalline porous semiconductor film on a transparent conductive glass as the photoanode. (ii) A platinum film with high electrocatalytic activity coated on a conductive glass as the cathode and (iii) a redox couple, frequently iodide/tri-iodide dissolves in an organic solvent as the electrolyte. The semiconductor photoanode is considered a key component in influencing the energy conversion efficiency of DSSCs. For the photoanodes composed of films of porous TiO_2 nanoparticles, dye adsorption is significantly enhanced on the large active surface, which in turn increases the amount of absorbed light. Throughout the illumination process, electrons are excited from the adsorbed dye on nano-TiO_2 particles and inserted into its conduction band, which is in contact with the electrolyte. Consequently, the electrons migrate into the back contact and stream in the outer path. At the same time, redox species in the electrolyte carry the formed holes from the oxidized dye molecules to the counter electrode. For this whole photoexcitation process to happen, light absorption needs to happen in the short wavelength region (UV-section) due to the large band gap energy of TiO_2 (3.2 eV).[4] However, TiO_2 has a small absorption coefficient in the light spectrum range of the visible region and near-infrared area, which considerably limits the amount of absorbed daylight.[5] In this manner, the photocurrent generation from daylight is not very valuable because most of the solar spectrum lies in the visible and near-IR regions. Subsequently, it is essential to change the photoresponse of TiO_2 so that its light absorption can cover the visible range. Accordingly, creating TiO_2 nanoparticles with wide photoresponse and high charge transportation is essential to enhance the DSSCs efficiency. Recently, several attempts have been done to modify nanostructured TiO_2 based photoanodes by different dopants to enhance the photovoltaic efficiencies of DSSCs.[6–9] At the same time, a few publications have also centered around the impacts of the nonmetal elements such as nitrogen and sulfur on the operation of the doped TiO_2 and the photovoltaic performing of the DSSCs.[10–14] In this manner, it is important to find a simple procedure for the fabrication and integration of nonmetal doped TiO_2 electrodes. The charge collection efficiency in DSSCs can be additionally enhanced by incorporation good conducting materials, such as graphene into TiO_2.[15,16] Graphene, is a two-dimensional nanomaterial with one-atom thickness, low resistance and excellent optical transmittance.[17] It was found that a combination of graphene with TiO_2 (P25) induced the development in the rutile phase and the porosity of TiO_2-photoelectrodes, accordingly improving the effectiveness of the DSSC by 14.9% in comparison with that of pure TiO_2 (P25).[18] To date, DSSCs utilizing graphene-TiO_2 as photoanodes were not carefully characterized in the literature.

The aim of this work is to evaluate the benefit of using visible light active N-doped TiO_2, synthesized by a simple economical method, such as a photoelectrode in dye-sensitized solar cells. The impact of N-content on the efficiency of fabricated DSSCs using N719 dye was studied. Also, the impact of modifying both pure and N-doped electrodes with graphene on the efficiency of fabricated cells was investigated.

EXPERIMENTAL

Materials

All chemicals used in this work were reagent grade. Double distilled water was used in all the experiments.

Synthesis of Pure and N-Doped TiO_2

In a typical synthetic method, 40 mL of $TiCl_4$ (BDH) was added dropwise into 20 mL of distilled water in an ice-water bath with magnetic stirring. After stirring for 1 h, the pH of the solution was adjusted to 8 by using diluted ammonia solution. The precipitate gotten was left for 1 h, filtered and washed carefully with water until Cl^- was not found. Finally, the precipitate was dried for 17 h at 110°C and calcined at 500°C for 4 h.

N-doped TiO_2 nanoparticles were prepared by mechanical mixing technique utilizing ammonium bicarbonate $(NH_4)HCO_3$ (BDH) as a source of nitrogen. In the synthetic process, 2 g of TiO_2 was firstly dispersed in deionized water and stirred for 30 min at room temperature. Subsequently, varied ammonium bicarbonate amounts were added with molar proportion: 20 wt.%, 40 wt.%, and 60 wt.% dropwise to the prepared solution under stirring at room temperature. After 2 h of stirring, the obtained mixture was transported into the Teflon-lined autoclave and heated at 105°C for 6 h. Ultimately, the sample was developed by annealing at 400°C for 6 h. These specimens were signified as N2-Ti, N4-Ti, and N6-Ti, for 20% N-doped TiO_2, 40% N-doped TiO_2, 60% N-doped TiO_2, respectively.

Synthesis of Reduced Graphene

Graphene oxide (GO) was prepared by a method described elsewhere.[19] one hundred and fifty milligrams of dispersed GO in 45 mL distilled water was sonicated for 1 h. Five milliliters of hydrazine hydrate was then added to the sonicated solution and heated at 98°C for 24 h. The dark reduced graphene powder acquired was finally collected by filtration and washed with distilled water a few times to take away the excessive hydrazine. The product obtained was then redistributed into the water and sonicated for 1 h. The suspended solution

was then centrifuged at 5000 rpm for 3 min to uproot bulk graphite. The last resultant powder was gathered by vacuum filtration and dried under vacuum.

Characterizations

The structure and composition of the powder samples were studied with x-ray powder diffractometer (XRD, Diano) with Cu *K* radiation (λ = 0.1541 nm). Ultraviolet-visible (UV-Vis) diffuse reflectance spectra for pure and N-doped TiO_2 were obtained with a UV-Vis spectrophotometer (UV-2550, Shimadzu). Fourier-transform infrared spectroscopy (FT-IR) spectra of the samples, in the range of 4000–400 cm^{-1}, were recorded on a Brucker-FTIR spectrophotometer model (Vector 22). The solid state samples were pressed into KBr pellets. The quality of the graphene was verified by Raman spectroscopy using a U-1000 laser Raman spectrometer by means of the 514.5 nm line of an ArC laser as the excitation beam. The textural properties of the materials investigated were determined by nitrogen adsorption technique using a Micromeritics ASAP 2020 adsorption device. Pore size and pore volume were computed by the BJH isotherm. X-ray photoelectron spectroscopy (XPS) was performed for chemical state analysis using a Perkin-Elmer RBD upgraded PHI-5300C ESCA system with monochromatic Mg-K excitation. A nonlinear least squares curve-fitting program (XPSPEAK software, Version 4.1) was used for XPS spectral deconvolution. An elemental analyzer was used to determine the atomic contents of nitrogen in doped samples. Moreover, the N amount in N6-Ti calculated from the peak of the N1s in XPS. The nitrogen content in N2-Ti, N4-Ti, and N6-Ti samples was found to be 0.71 at.%, 1.23 at.%, and 1.57 at.%, respectively.

Fabrication of DSSCs

TiO_2 electrodes were prepared by mixing 3 gm of the TiO_2 powder with 0.2 mL of Triton X-100 and 0.0912 poly(ethylene glycol) (PEG, Mw = 10,000) in 10 mL bidistilled water to form a viscous suspended solution. The suspended solution was spread on a piece of transparent conducting FTO glass (fluorine-doped tin oxide conductive glass sheet with a resistance of 10–15 Ohm cm^{-2}) by using doctor-blade technique. The specimen was then heated at 500°C for 1 h in the air, cooled to room temperature at once. For the preparation of graphene composite electrode, 0.2 wt.% of graphene was added to the suspended solution of TiO_2. After that, it was stirred for about 45 min to let graphene disperse uniformly in the suspension and anchor with the present TiO2. Next, the composite electrode was prepared in similar fashion as theTiO_2 electrodes. The final area of the electrode was about 1 cm^2. The formed photoelectrodes immersed in (0.0628 g L^{-1}) ethanolic N719 solution for 2 days. The excess of dye adsorbed on the top surface of electrodes was removed by washing with ethanol. Finally, a sandwich-type DSSC arrangement was made by creating an electrolyte layer between the N719 dye-loaded photoelectrode and the counter electrode, which consisted of the same conducting glass coated with graphite film. The electrolyte was constituted of 0.02 M of KI and I_2 in acetonitrile. The photocurrent-voltage (*I-V*) characteristic curves were measured using Keithley 2601 under AM1.5G illumination with an irradiation intensity of 100 mW cm^{-2}.

RESULTS AND DISCUSSION

X-Ray Diffraction

The XRD patterns for pure TiO_2 and its doped N-TiO_2 sample powders are shown in Fig. 1a. The XRD patterns of all specimens are attributed to pure anatase phase due to the appearance of the identified diffraction peaks at 2θ = 25.32°, 37.88°, 48.08°, 53.80°, 55.04°, and 62.80°, which are assigned to the (101), (004), (200), (105), (211), and (215) anatase crystal planes, respectively [Joint Committee on Powder Diffraction Standards (JCPDS) no. 21-1272]. The formation of anatase phase is valuable for our work because using the anatase phase as a photoanode in DSSCs is more equipped for converting solar energy than that of the rutile phase.[20] The average crystallite sizes of the samples calculated from the most intense diffraction peak (101) using the Debye–Scherrer mathematical statement[21] are found to lie in the range of 7.1–12.3 nm.

X-ray diffraction pattern of the prepared graphene is shown in Fig. 1b. It demonstrates high crystallinity peaks of graphene at around 2θ = 26.4º and 42.5º, corresponding to (002) and (100) hexagonal graphene planes,[22] respectively. No other reflection peaks, including the (001) plane of graphene oxide (GO) are observed, referring to the complete reduction of GO to reduced graphene oxide (rGO).

Fourier Transform Infra-Red Spectra (FTIR)

The FT-IR spectra of pure and nitrogen-doped TiO_2 samples with various nitrogen concentrations are given in Fig. 2. All the N-doped TiO_2 specimens exhibit bands at 3400 cm^{-1}, 3160–3280 cm^{-1}, 1880–1960 cm^{-1}, 1630–1640 cm^{-1}, 1440 cm^{-1}, 1080 cm^{-1} and 520 cm^{-1}. The broad band observed at 3400 cm^{-1} is assigned to O-H surface groups and H_2O-adsorbed molecules.[23] The wide and intense band at the 3160–3280 cm^{-1} is ascribed to the molecular stretching of NH itself.[24] The wide bands extending from 1880–1960 cm^{-1} refer to the stretching of N-N buildings of the N species exist in the N-doped specimens. The band at $\sim$ 1630 cm^{-1} relates to twisting vibrations of O-H and N-H.[25,26] The band at 1440 cm^{-1} can be credited to the

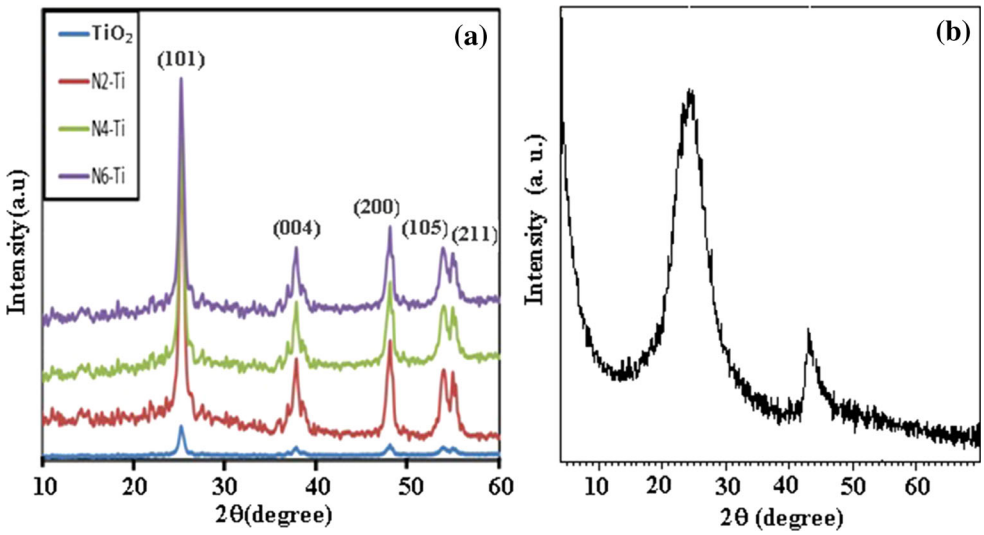

Fig. 1. XRD patterns of (a) pure and N-doped TiO_2 samples and (b) grapheme.

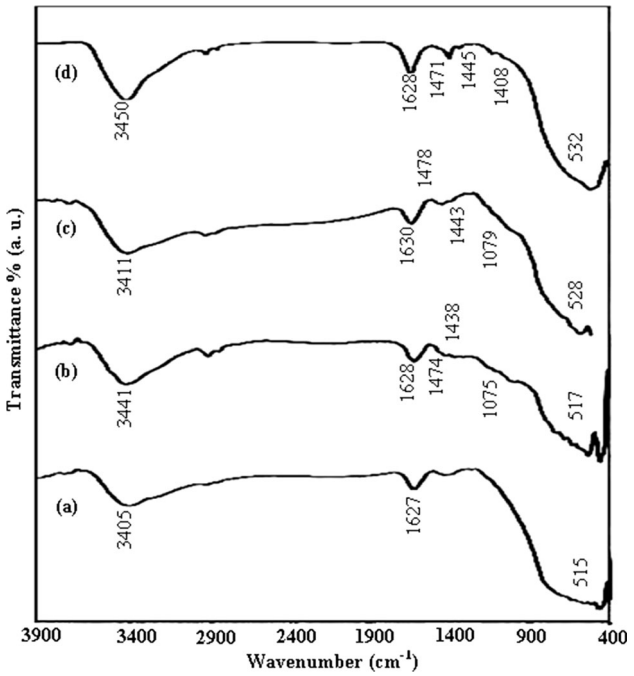

Fig. 2. FT-IR spectra of (a) TiO_2, (b) N2-Ti, (c) N4-Ti, and (d) N6-Ti.

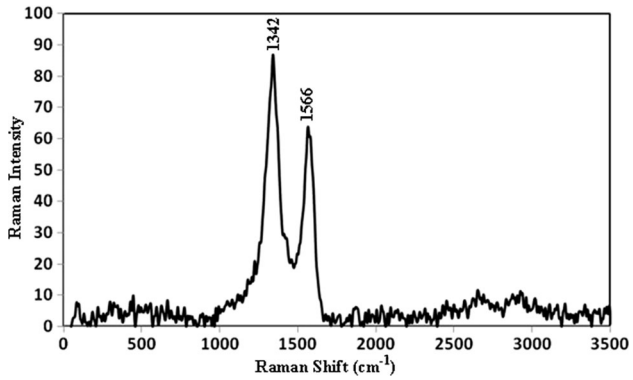

Fig. 3. Raman spectrum of reduced graphene oxide.

nitrogen atoms substitute into TiO_2 network.[27] This peak originates from N-H bending.[28] The peak at 1079 cm^{-1} is assigned to the vibration of Ti-N bond because of entering nitrogen species in TiO_2 network.[29,30] The spectra of both the N-doped and pure TiO_2 specimens also show an intense band situated at ~ 520 cm^{-1} assigned to Ti-O stretching and Ti-O-Ti bridging stretching modes.[31]

Raman Spectrum

The Raman spectrum of the synthesized graphene is shown in Fig. 3. The figure shows two major peaks, specifically D band and G band at 1342 cm^{-1} and 1566 cm^{-1}, respectively. The G band is accredited to all sp2 carbon forms and is responsible for the in-plane vibration of sp2 bonded carbon atoms while the D band implies the presence of sp3 defects. Moreover, the relative strength of the D band compared to the G band hangs on the extent of disorder in the graphitic materials.[32]

Optical Properties

Figure 4a and b demonstrates the optical absorbance and diffuse reflectance spectra of pure TiO_2 and its nitrogen-doped TiO_2 with distinctive doping concentrations. The optical absorbance data were calculated from the reflection data by applying the Kubelka-Munk function, as assumed by equation[33]:

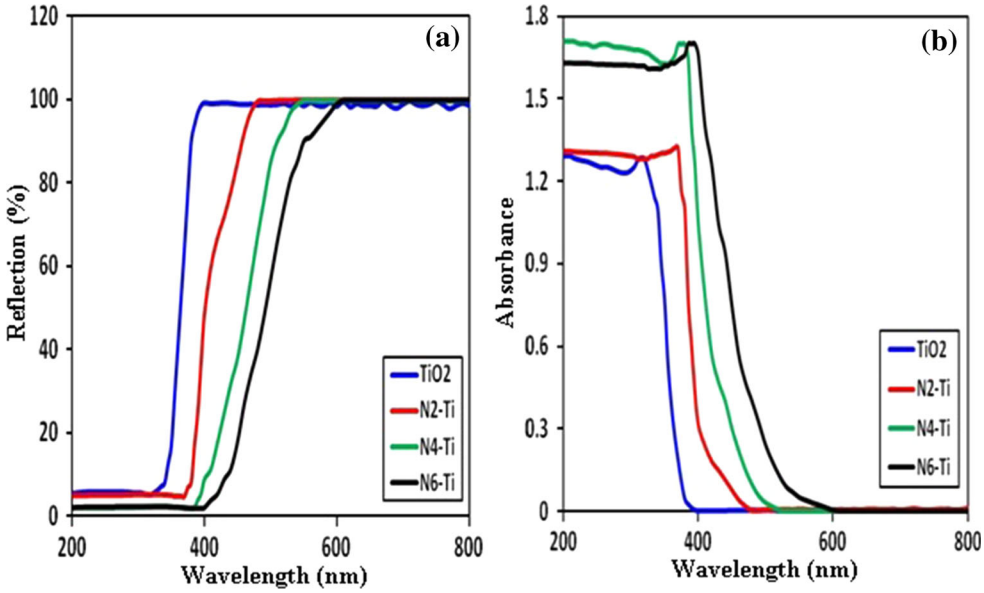

Fig. 4. Optical properties of investigated samples. (a) Reflection spectra of N6-Ti, N4-Ti, N2-Ti, and pure TiO_2. (b) Absorption spectra of N6-Ti, N4-Ti, N2-Ti, and TiO_2 (Color figure online).

Table I. Optical data of the studied samples

Sample	Wt.% of nitrogen in TiO_2	Optical absorption edge $\lambda_{(nm)}$	Energy gap E_g (eV), indirect transition	R^2	Energy gap E_g (eV), direct transition	R^2
TiO_2	0	400	3.18	0.998	3.53	0.993
N2-TiO_2	0.71	460	3.12	0.997	3.61	0.993
N4-TiO_2	1.23	490	3.00	0.998	3.41	0.994
N6-TiO_2	1.57	570	2.70	0.998	3.15	0.994

$$F(R) = (1-R)^2/(2R) \quad (1)$$

where R is the ratio of sample reflectance to the reference reflectance.[33] Figure 4 illustrates that the visible light absorptions of doped samples are higher than that of the pure one. The maximum wavelengths at which the absorption was obtained are recorded in Table I. The absorbance threshold of N-doped TiO_2 shifts to a higher wavelength by increasing the nitrogen amount in the sample. This shift is because a few nitrogen atoms are embedded into TiO_2 lattice producing hybrid orbitals of N2p and O2p and arranging new valence band. This band moves to the conduction band of TiO_2 and causes the gap energy to be smaller. Consequently, the optical absorption of N-doped TiO_2 demonstrates a red shift; this means that the implantation of nitrogen atoms into TiO_2 lattice extends its light absorption range.

The optical band gap energy (Eg) has been concluded using the Tauc relation,[34] which is given by:

$$(\alpha h\nu)^{1/n} = A(h\nu - E_g) \quad (2)$$

where α is absorption coefficient and n depends on the type of transition (n = 1/2 for indirect transition and n = 2 for direct transition), h is the Planck constant, and ν is the frequency of photons. The type of band gap transition occurring in our samples was determined by fitting the experimental absorption spectra to Eq. 2. The E_g-values were determined by the extrapolation of best fit lines using a graphic presentation of $(\alpha h\nu)^n$ to intercept with the phonon energy ($h\nu$) axis, and the values obtained are listed in Table I. For the indirect transition, the samples show a much better fit than the corresponding indirect band gap fit and produce an E_g value of 3.18 eV for undoped TiO_2 , which is in good agreement with the reported values in the literature.[35] Table I shows that nitrogen introduction into TiO_2 lattice leads to lower E_g-value either by direct or indirect allowed transitions. This is attributed to the formation of new hybrid orbital from N2p and O2p orbital, as mentioned before.

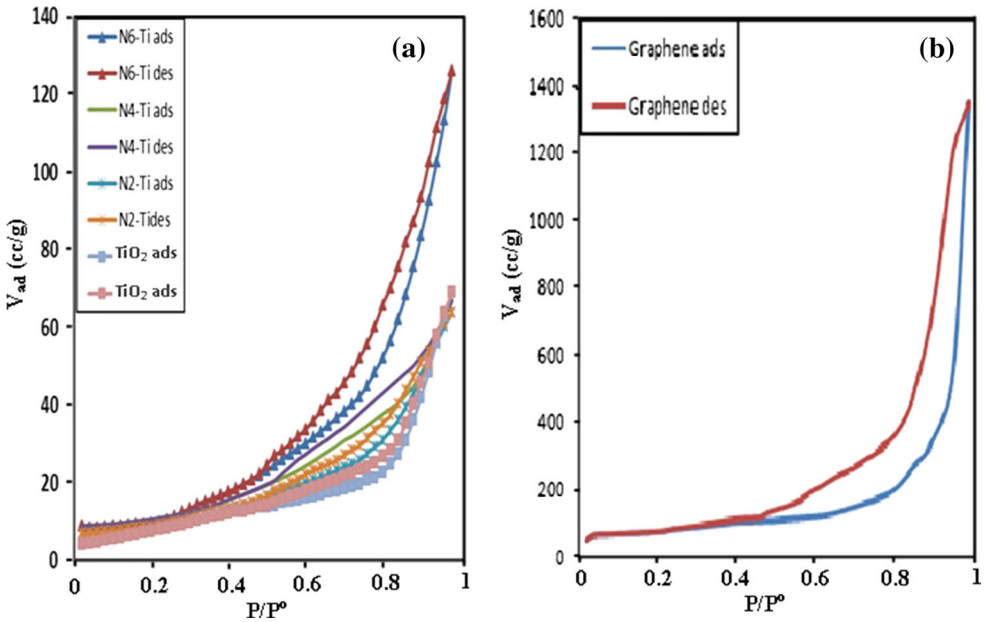

Fig. 5. N_2-adsorption/desorption isotherm curves of (a) pure and N-doped TiO_2 samples and (b) graphene.

Table II. Textural data of the studied samples

Sample	Content of nitrogen (wt.%) in TiO_2	Pore volume (cc g^{-1})	Pore radius (nm)	SBET (m^2 g^{-1})
TiO_2	0	0.12	7.0	39.5
N2-Ti	0.71	0.11	7.6	41.1
N4-Ti	1.23	0.11	7.8	43.1
N6-Ti	1.57	0.21	13.6	45.6

Surface Area Measurement

The N_2-adsorption/desorption isotherms for the pure and N-doped TiO_2 specimens are presented in Fig. 5. According to IUPAC classification, the adsorption/ desorption plots show a sort IV isotherm curve with an H2 hysteresis loop,[36] which means the material has mesoporous structure. The surface area and pore volume of the studied materials were calculated and recorded in Table II. The table shows that both the specific surface area and pore diameter increase by increasing the nitrogen content in the investigated material. This denotes that the incorporation of nitrogen doping effectively stabilized the TiO_2 particles and hindered their agglomeration.[37]

XPS

In order to get the structure and the chemical state data, XPS measurements were performed for pure and N-doped TiO_2 containing the highest content of nitrogen (N6-Ti). The wide-scan XPS spectra acquired are indicated in Fig. 6a and b. The peaks observed in the spectra were assigned to C, O, Ti elements, in addition to a clear nitrogen signal in the spectrum of N-doped specimen. The presence of the C1s peak might be credited to the current existence of carbon in the environment.

Figure 6c, d, e, and f shows high-resolution XPS spectra of the Ti 2p, N1s, and O1s regions of the pure and N6-Ti samples. The spectrum of pure TiO_2 (Fig. 6c) demonstrates two peaks at 465.6 eV and 459.5 eV, which are the specific binding energy (BE) of Ti^{4+} 2p1/2 and Ti^{4+} 2p3/2, respectively, while the related 2p peaks of the N-doped specimen are seen at lower BE of 463.2 eV and 458.7 eV (Fig. 6d). These red shifts in binding energies reveal that the electronic interaction of Ti with anions in N-TiO_2 is not quite the same as that in pure TiO_2. It infers that TiO_2 crystal lattices are adjusted with substitutional and/or interstitial N atoms, consequently, fractional Ti may be affected by an electronic interaction with nitrogen. The lesser electronegativity of nitrogen [Pauling's electronegativity (3.04)] compared with oxygen (3.44) decreased the percent ionicity and electron intensity over N anion, and thus electron intensity on Ti enlarged.[38] Therefore, the BE of Ti2p decreases with nitrogen doping. The

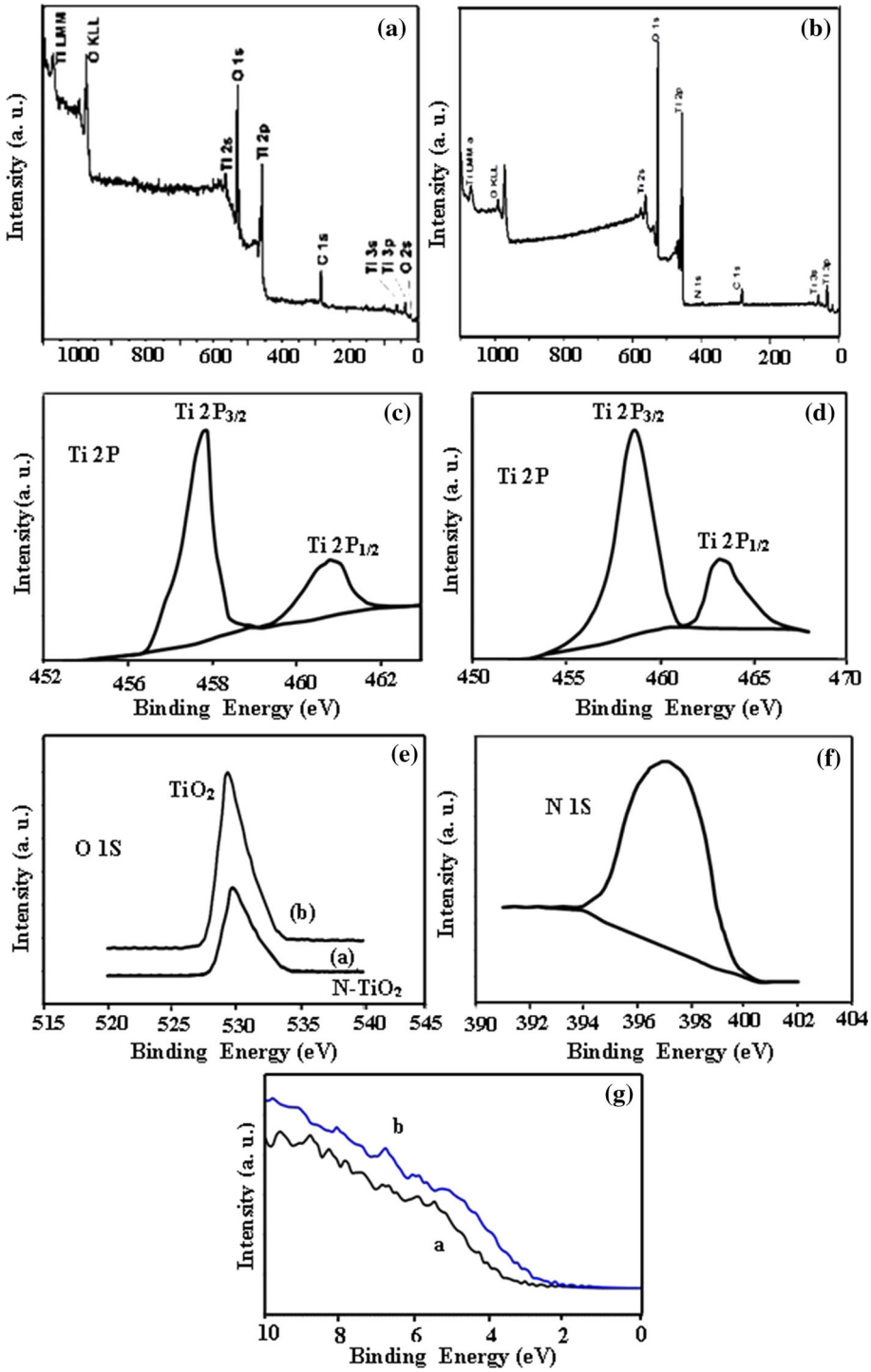

Fig. 6. XPS spectra of (a) TiO_2 and (b) 6 N-Ti samples (survey), and high-resolution XPS spectra for (c, d) Ti 2p, (e) O1s, and (f) N1s. (g) Valence band XPS spectra of *a*, TiO_2 and *b*, N6-Ti.

nitrogen found in doped-TiO_2 can present in two species arrangements: interstitial nitrogen (Ti-O-N) or substitution nitrogen (O-Ti-N). It was registered that the formation of nitrogen in interstitial position (Ti-O-N-like species) is not joined by narrowing in band gap energy,[27,39] which is not seen in our results. In this way, nitrogen was suggested to be formed in the substitution position.

In Fig. 6f, the XPS spectrum of the N-doped sample demonstrates a peak at 397.1 eV for N1s core level. This reflects the formation of N-Ti-O bonds, which indicates the substitution of N-ion for

O-ion.[40–43] The BE of O1s core level is shown in Fig. 6e. It is worth noting that the peak of oxygen is shifted from lower energy state 529.8 eV for pure TiO_2 to 529.4 eV for N-TiO_2. This shift may be identified with the formation of oxygen vacancies as a result of the nitrogen doping.[44] The change observed in BE of both O1s and N1s regions denote that nitrogen is incorporated into the TiO_2 lattice. The shifts in BE of Ti 2p3/2 and O1s peaks originally come from the formation of oxygen vacancies in the TiO_2 lattice.[45]

Generally, these results reveal that the creation of oxygen vacancy is joined by nitrogen doping and the optical transitions between the dopant-induced hybrid level and Ti-3d orbital elucidate the detected visible light absorptions of N-TiO_2 samples.

To further understand the shift occurring in the absorption spectra due to the implantation of nitrogen in TiO_2. The density of states (DOS) of the valence band of pure TiO_2 and 6-NTi samples were measured by valence band XPS (Fig. 6g). From the XPS spectra, the pure TiO_2 demonstrated a valence band maximum (VBM) at 3.1 eV, whereas, the nitrogen-doped sample N6-Ti exhibited a VBM at 2.2 eV, demonstrating a shift of 0.9 eV due to the nitrogen doping. The change of VBM implies the rise of absorption capability in the visible light regime. However, these results denote the effective activation of visible-light photoactivity produced by nitrogen doping.

Photovoltaic Characteristics of the DSSCs

Based on these results, which showed higher optical absorption in the visible region, DSSCs with different anodes were fabricated and compared. The four tested anodes were pure TiO_2, N6-Ti (containing the highest doping amount of nitrogen atom), TiO_2/graphene and N6-Ti/graphene.

The current density-voltage (J-V) characteristics of the prepared cells with N719 as sensitizer are shown in Fig. 7. In view of the J-V characteristics of the DSSCs, the fill factor (FF) and η were calculated using the relations[44]:

$$FF = (V \times J_{max})/(V_{oc} \times J_{oc}) \quad (3)$$

$$\eta = (V_{oc} \times J_{oc} \times FF)/(P_{in}) \quad (4)$$

where, J is the photocurrent density and V is the photovoltage for maximum power output; J_{sc} and V_{oc} are the short-circuit photocurrent density and open-circuit photovoltage, respectively. The P_{in} is the power of the incident light, and A is the active area of the cell. The photovoltaic parameters are listed in Table III from which it is observed that the efficiency (η) increases by introducing nitrogen into the TiO_2 photoanode. This increase can be explained on the basis of expanding the amount of light absorbed in the visible range by introducing nitrogen into TiO_2 lattice, as specified previously. Moreover, the larger surface areas and the increase in pore volume of the N-doped TiO_2 film can enlarge

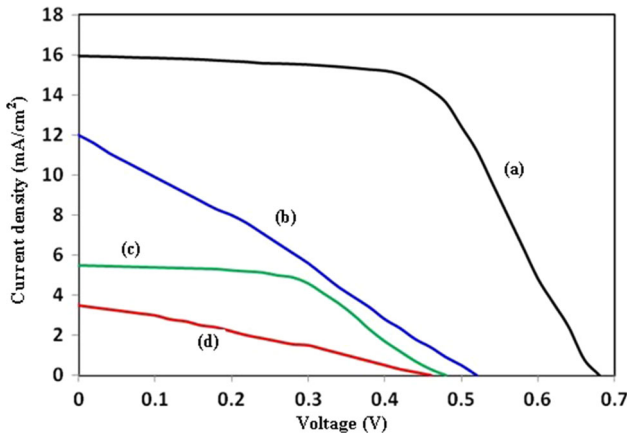

Fig. 7. I-V characteristic of the investigated samples: (a) N6-Ti/-graphene, (b) TiO_2/graphene, (c) N6-Ti, and (d) TiO_2.

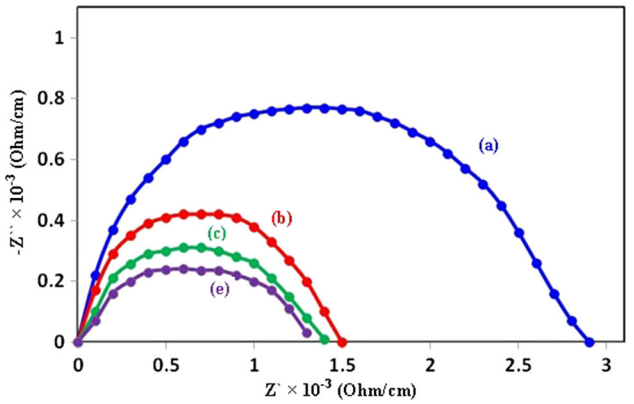

Fig. 8. Impedance spectra of the investigated samples: (a) TiO_2, (b) N6-Ti, (c) TiO_2/graphene, and (d) N6-Ti/graphene.

Table III. Photoelectrochemical data obtained from DSSCs based on N719 dye with different TiO_2 nanoparticles

Solar cell	J_{max} (mA cm^{-2})	V_{max} (V)	I_{sc} (mA cm^{-2})	V_{oc} (V)	Fill factor *FF*	Efficiency (%)
TiO_2	1.80	0.23	3.50	0.46	0.257	0.41
N6-Ti	5.05	0.24	5.50	0.47	0.470	1.21
TiO_2/G	6.80	0.27	12.0	0.52	0.294	1.84
N6-Ti/G	15.04	0.42	15.93	0.68	0.582	6.30

the quantity of dye adsorbed and additional prompt a multiplication in the conversion efficiency of the DSSCs.

The photovoltaic characteristics of DSSCs with graphene demonstrate an increase in the photocurrent as compared to the other studied DSSCs, Table III. The improvement in the charge transport efficiency is the reasonable explaining for the upgraded J_{sc} in the DSSC containing graphene. This may be attributed to the very high electron mobility of graphene (10^4 cm^2 V^{-1} s^{-1} at room temperature) making it a promising material for electron transport channels.[46] Subsequently, graphene works in our cell as a bridge between the TiO_2 particles and captures the charges in TiO_2 and rapidly transports them to the following TiO_2 particles. In this way, charges transportation distances are reduced, charges recombination is controlled, and the J_{oc} of DSSCs is improved. Also, since TiO_2 conduction band is at lower energy than its fermi level,[47,48] thus the photogenerated electrons in the TiO_2 have a tendency to insert into graphene and then transport to conductive glass rapidly, whereas holes halt in the valence band of TiO_2. In this way, the recombination probability of electron-hole pairs in the working layer put down by including the graphene film. The presence of graphene layer caused an increase in the open-circuit voltage (V_{oc}); therefore, we can say that the back-transfer of electrons from the FTO electrode to the I_3^- ions put down by the arrangement of graphene-TiO_2 interfacial layer. Enhancement of the performance of DSSCs by introducing the graphene layer is expected as a result of delaying the charge recombination and the fast transportation of the photoelectrons to the external circuit. The work function of the graphene (4.42 eV) lies between the conduction band of TiO_2 (4.4 eV), and FTO glass (4.7 eV), which facilitates the transition of photogenerated electrons from TiO_2 to FTO.[49] The average band gap of graphene gives force in energy levels, which helps compelling charge division and transport of photoelectrons to electrodes. This suggests that the pores presented through the incorporation of graphene may act as light-collecting centers.[50] In this way, the introduction of graphene into TiO_2 photoanode co-operates the major part in the photovoltaic performance of DSSC.

To further study the impact of N doping photoelectrochemical procedures happening in DSSCs, EIS was performed, Fig. 8. The figure shows that for each DSSC the Nyquist plot demonstrates one semicircle. The single arc is due to the resistance of the charge-transfer process taking place at TiO_2/dye/electrolyte interface. The radius of the semicircles decreases by introducing nitrogen into TiO_2. The reduction in resistance is due to that the electron is easy to be transferred to the underlying TiO_2 (from 2.9 Ohm cm^{-1} to 1.5 Ohm cm^{-1}), which results in the enhanced electron injection and increased conversion efficiency in DSSC. It ought to be specified here that the impedance value of the DSSC containing graphene is lower than the other cells. This refers to the enhancement of the electron transport between the TiO_2 nanoparticles and I_3^- in the electrolyte after mixing with graphene. This causes proposing faster electron transference of charge carriers and more operative electron-hole pairs split attained over the electrodes containing graphene as compared to that without graphene. This result is also confirmed by the *J-V* plots where the current density (*J*) is associated with the electron transfer rate of the electrode materials. The higher *J*-values gained by graphene/TiO_2 electrodes reveals that better electron transfer is attained over the DSSCs device.

The electron lifetime τ of fabricated DSSCs was calculated as the reciprocal of the characteristic maximum frequency peak ($\tau = 1/\omega_{max}$)[51,52] based on the collected EIS data. Graphene incorporation facilitated electron transport[53] as confirmed by the higher electron lifetime of both DSSC samples with graphene layer (N6-Ti/graphene and TiO_2/graphene) compared to their counterparts with no graphene (N6-Ti and TiO_2). Besides improving its transport, graphene decreased electrons recombination with the oxidized dye or electrolyte species by offering a lower resistance path than that of TiO_2.

CONCLUSION

In conclusion, we studied the impacts of nitrogen incorporation on the properties of hydrothermally synthesized nano-crystalline TiO_2. The results showed that N-doped TiO_2 samples were of higher surface areas and pore volumes, as well as smaller band gap energies than those of pure TiO_2. The improved material properties due to high nitrogen incorporation in the bulk of TiO_2 lattice had a direct impact on the photovoltaic behavior of fabricated N-doped DSCCs. We found that while N-doping led to a $\sim 3\times$ increase in fabricated DSSC energy conversion efficiency, the addition of graphene layer improved it further to $15\times$ higher than achieved value using pure TiO_2 cell. This improvement is attributed to the high conductivity of graphene causing an enhancement in photoelectron transfer and a decrease in charge recombination as confirmed by the presented EIS analysis.

CONFLICT OF INTEREST

The authors declare that they have no conflict of interest.

REFERENCES

1. X. Pengtao, N.S. McCool, and T.E. Mallouk, *Nano Today* 14, 42 (2017).
2. S. Suhaimi, M.M. Shahimin, Z.A. Alahmed, J. Chyský, and A.H. Reshak, *Electroch. Appl.* 10, 2859 (2015).
3. Z. Jin, M. Zhang, M. Wang, Ch Feng, and Z. Wang, *Acc. Chem. Res.* 50, 895 (2017).
4. S. Kavitha, K. Praveena, and M. Lakshmi, Int. J. Energy Res. (2017). https://doi.org/10.1002/er.3778.

5. J. Gong, K. Sumathy, Q. Qiao, and Z. Zhou, *Renew. Sustain. Energy Rev.* 68, 234 (2017).
6. T. Sakthivel, K.A. Kumar, J. Senthilselvan, and K. Jagannathan, *J. Mater. Sci. Mater. Electron.* 29, 2228 (2018).
7. R.S. Dubey and Sh Singh, *Results Phys.* 7, 1283 (2017).
8. G.M. Abed, A.M.A. Alsammarraie, and B.I. Al-Abdaly, *Nanosci. Nanometr.* 3, 27 (2017).
9. Y. Duan, N. Fu, Q. Liu, Y. Fang, X. Zhou, J. Zhang, and Y. Lin, *J. Phys. Chem. C* 116, 8888 (2012).
10. V.A. Tran, T.T. Truong, T.A.P. Phan, T.N. Nguyen, T.V. Huynh, A. Agresti, S. Pescetelli, T.K. Le, A.D. Carlo, T. Lund, S. Le, and P.T. Nguyen, *Appl. Surf. Sci.* 399, 515 (2017).
11. M.Y.A. Rahman, A.A. Umar, S.K.M. Saad, M.M. Salleh, and A. Ishaq, *J. New Mater. Electrochem. Syst.* 17, 33 (2014).
12. L.Q. Ping, *Appl. Mech. Mater.* 548, 264 (2014).
13. H. Seo, S. Nam, N. Itagaki, K. Koga, M. Shiratani, and J. Boo, *Electron. Mater. Lett.* 12, 530 (2016).
14. M.G. Fischer, X. Hua, B.D. Wilts, I. Gunkel, T.M. Bennett, and U. Steiner, *ACS Appl. Mater. Interfaces* 9, 22388 (2017).
15. L. Liu, Y. Zhang, B. Zhang, and Y. Feng, *J. Mater. Sci.* 52, 58070 (2017).
16. J.D. Roy-Mayhew and I.A. Aksay, *Chem. Rev.* 114, 6323 (2014).
17. X. Li, I. Chu, X. Zhang, and H. Cheng, *Phys. Rev. B* 91, 195442 (2015).
18. J. Song, Z. Yin, Z. Yang, P. Amaladass, S. Wu, J. Ye, Y. Zhao, W. Deng, H. Zhang, and X. Liu, *Chem. A Eur. J.* 17, 10832 (2011).
19. J. Chen, B. Yao, C. Li, and G. Chi, *Carbon* 64, 225 (2013).
20. K. Usha, B. Mondal, D. Sengupta, P. Das, K. Mukherjee, and P. Kumbhakar, *Nanosci. Nanoeng.* 2, 29 (2014).
21. H.P. Klug and L.E. Alexander, *X-Ray Diffraction Procedures for Polycrystalline and Amorphous Materials* (New York: Wiley, 1970).
22. B.K. Saikia, R. Boruaha, and P.K. Gogoi, *J. Chem. Sci.* 121, 103 (2009).
23. K.L. Yeung, S.T. Yau, A.J. Maira, J.M. Coronado, J. Soria, and P.L. Yue, *J. Catal.* 219, 107 (2003).
24. G. Socrates, *Infrared and Raman characteristics group frequencies: Tables and charts*, 3rd ed. (New York: Wiley, 2001).
25. J. Geng, D. Yang, J. Zhu, D. Chen, and Z. Jiang, *Mater. Res. Bull.* 44, 146 (2009).
26. M. Primet, P. Pichat, and M.-V. Mathieu, *J. Phys. Chem.* 75, 1216 (1971).
27. J. Geng, D. Yang, J. Zhu, D. Chen, and Z. Jiang, *Mater. Res. Bull.* 44, 146 (2009).
28. T. Matsumoto, N. Iyi, Y. Kaneko, K. Kitamura, S. Ishihara, Y. Takasu, and Y. Murakami, *Catal. Today* 120, 226 (2007).
29. S. Shanmugasundaram, J. Marcin, and H. Kisch, *J. Phys. Chem. B.* 108, 19384 (2004).
30. H. Li, J. Li, and Y. Hou, *J. Phys. Chem. B.* 110, 1559 (2006).
31. D. Huang, S. Liao, S. Quan, L. Liu, Z. He, J. Wan, and W. Zhou, *J. Mater. Res.* 22, 2389 (2007).
32. Y.Y. Wang, Z.H. Ni, T. Yu, Z.X. Shen, and H.M. Wang, *J. Phys. Chem. C* 112, 10637 (2008).
33. R. Lopez and R. Gomez, *J. Sol-Gel. Sci. Technol.* 61, 1 (2012).
34. J. Tauc, R. Grigorovici, and A. Vancu, *Phys. Status Solidi (b)* 15, 627 (1966).
35. Z. Essalhi, B. Hartiti, A. Lfakir, M. Siadat, and P. Thevenin, *J. Mater. Environ. Sci.* 7, 1328 (2016).
36. M.D. Donohue and G.L. Aranovich, *Adv. Colloid Interface Sci.* 76–77, 137 (1998).
37. M.T. Harris, R.R. Brunson, C.H. Byers, and J. Non-Cryst, *Solids* 121, 397 (1990).
38. Z.P. Wang, W.M. Cai, X.T. Hong, X.L. Zhao, F. Xu, and C.G. Cai, *Appl. Catal. B Environ.* 57, 223 (2005).
39. D. Nassoko, Y.F. Li, H. Wang, J.L. Li, Y.Z. Li, and Y. Yu, *J. Alloys Compd.* 540, 228 (2012).
40. H. Irie, Y. Watanabe, and K. Hashimoto, *J. Phys. Chem. B* 107, 5483 (2003).
41. O. Diwald, T.L. Thompson, E.G. Goralski, S.D. Walck, and J.T. Yates, *J. Phys. Chem. B* 108, 6004 (2004).
42. J.M. Mwabora, T. Lindgren, and E. Avendaño, *J. Phys. Chem. B* 108, 20193 (2004).
43. C.D. Valentin, G. Pacchioni, A. Selloni, S. Livraghi, and E. Giamello, *J. Phys. Chem. B* 109, 11414 (2005).
44. Q. Wang, S. Ito, M. Gratzel, F. Fabregat-Santiago, I. Mora-Sero, J. Bisquert, T. Bessho, and H. Imai, *J. Phys. Chem. B* 110, 25210 (2006).
45. J. Wang, D.N. Tafen, and J.P. Lewis, *J. Am. Chem. Soc.* 131, 12290 (2009).
46. T. Stauber, N.M.R. Peres, and F. Guinea, *Phys. Rev. B* 76, 205423 (2007).
47. A. Adán-Más and D. Wei, *Nanomaterials* 3, 325 (2013).
48. R. Beranek, Adv. Phys. Chem. ID786759 (2011).
49. A. Zaban, *J. Phys. Chem. Lett.* 4, 2822 (2013).
50. X. Lu, X. Mou, J. Wu, D. Zhang, L. Zhang, F. Huang, F. Xu, and S. Huang, *Adv. Funct. Mater.* 20, 509 (2010).
51. Y. Zhao, X. Li, Q. Li, and C. Deng, *J. Mater. Sci. Technol.* 27, 764 (2011).
52. Q. Ang, Z. Zhang, S. Zakeeruddin, and M. Grätzel, *J. Phys. Chem. C* 112, 7084 (2008).
53. M. Toivola, J. Halme, K. Miettunen, K. Aitola, and P.D. Lund, *Int. J. Energy Res.* 33, 1145 (2009).